The Astrophysical Journal, 704:1107–1119, 2009 October 20 doi:10.1088/0004-637X/704/2/1107

DISCOVERY OF A TRANSITING PLANET AND EIGHT ECLIPSING BINARIES IN HATNet FIELD G205*

David W. Latham[1], Gáspár Á. Bakos[1,9], Guillermo Torres[1], Robert P. Stefanik[1], Robert W. Noyes[1], Géza Kovács[2], András Pál[1,3], Geoffrey W. Marcy[4], Debra A. Fischer[5], R. Paul Butler[6], Brigitta Sipőcz[1,3], Dimitar D. Sasselov[1], Gilbert A. Esquerdo[1], Steven S. Vogt[7], Joel D. Hartman[1], Gábor Kovács[1], József Lázár[8], István Papp[8], and Pál Sári[8]
[1] Harvard-Smithsonian Center for Astrophysics, 60 Garden Street, Cambridge, MA 02138, USA
[2] Konkoly Observatory, Budapest, Hungary
[3] Department of Astronomy, Eötvös Loránd University, Budapest, Hungary
[4] Department of Astronomy, University of California, Berkeley, CA 94720, USA
[5] Department of Physics and Astronomy, San Francisco State University, San Francisco, CA 94132, USA
[6] Department of Terrestrial Magnetism, Carnegie Institution of Washington, 5241 Broad Branch Road NW, Washington, DC 20015-1305, USA
[7] University of California Observatories/Lick Observatory, University of California, Santa Cruz, CA 95064, USA
[8] Hungarian Astronomical Association, Budapest, Hungary
Received 2008 November 25; accepted 2009 August 28; published 2009 September 30

ABSTRACT

We report the discovery of HAT-P-8b, a transiting planet with mass $M_{\rm p} = 1.52^{+0.18}_{-0.16}\ M_{\rm J}$, radius $R_{\rm p} = 1.50^{+0.08}_{-0.06}\ R_{\rm J}$, and photometric period $P = 3.076$ days. HAT-P-8b has a somewhat inflated radius for its mass, and a somewhat large mass for its period. The host star is a solar-metallicity F dwarf, with mass $M_\star = 1.28 \pm 0.04\ M_\odot$ and $R_\star = 1.58^{+0.08}_{-0.06}\ R_\odot$. HAT-P-8b was initially identified as one of the 32 transiting-planet candidates in HATNet field G205. We describe the procedures that we have used to follow up these candidates with spectroscopic and photometric observations, and we present a status report on our interpretation for 28 of the candidates. Eight are eclipsing binaries with orbital solutions whose periods are consistent with their photometric ephemerides; two of these spectroscopic orbits are single-lined and six are double-lined.

Key words: planetary systems – stars: individual (HAT-P-8, GSC 02757-01152) – techniques: spectroscopic

Online-only material: color figure, machine-readable tables

1. INTRODUCTION

Photometric surveys are now finding many hundreds of stars that exhibit periodic dimmings that look like they might be due to transiting planets, but so far the vast majority of these candidates have turned out to be stellar systems involving eclipsing binaries and not planets. To make a convincing case that the light curve is due to a transiting planet it is necessary, but not sufficient, to show that the detailed shape of the dimming, including depth and duration, can be accurately modeled as a planet. Confirmation that the unseen companion is a planet requires an orbit for the host star that matches the photometric ephemeris and implies a planetary mass for the companion. For a spectroscopic orbit, it is also necessary to demonstrate that the measured velocity variations are not due to astrophysical effects other than orbital motion.

At the Harvard-Smithsonian Center for Astrophysics (CfA), we have been following up transiting-planet candidates identified by wide-angle ground-based photometric surveys for almost 10 years, starting with targets supplied by the Vulcan team in 1999. We quickly learned that the Vulcan sample was dominated by systems involving eclipsing binaries (Latham 2003). Indeed, we have not yet been able to confirm that any of the 66 Vulcan candidates that we observed are actually planets. More recently, two other wide-angle surveys, TrES and HATNet, have been the source of a large number of transiting-planet candidates that have been followed up spectroscopically, initially at CfA. As of 2009 July 1, a total of 871 candidates from these two surveys had been observed, with a total of 17 published as confirmed planets and several more in preparation for publication.

Over the years our procedures for reducing and analyzing our photometric data and for identifying good transiting-planet candidates have considerably evolved, and we have encountered a variety of stellar systems that can mimic transiting planets. Thus, one of the goals of this paper is to report our present procedures and some of the lessons learned. A second goal is to document the false positives that we have identified in the process of our work to follow up candidates identified in HATNet field G205, to provide examples of the types of false positives that we have encountered. These two goals are addressed in Sections 2 and 3. Finally, in Section 4 we characterize HAT-P-8b, the second transiting planet to be discovered in HATNet field G205.

2. PHOTOMETRIC DETECTION

The HATNet telescopes HAT-5, HAT-6, HAT-8, and HAT-9 (HATNet; Bakos et al. 2002, 2004) observed HATNet field G205, centered at $\alpha = 22^{\rm h}56^{\rm m}$, $\delta = +37^\circ30'$, on a nightly basis between 2003 September 29 and 2004 February 1, and between 2006 July 3 and 2006 July 24. Exposures of 5 minutes were obtained at a 5.5-minute cadence whenever conditions permitted; all in all 4460 exposures were secured, each yielding photometric measurements for approximately 45,000 stars in the field down to $I \sim 14.0$ mag. The field was observed in network mode, exploiting the longitude separation between HAT-5/6, stationed at the Smithsonian Astrophysical Observatory's (SAO) Fred Lawrence Whipple Observatory (FLWO) on Mount Hopkins in Arizona ($\lambda = 111^\circ$W), and HAT-8/9, installed on the rooftop of SAO's Submillimeter Array building atop Mauna Kea, Hawaii ($\lambda = 155^\circ$W).

* Based in part on observations obtained at the W. M. Keck Observatory, which is operated by the University of California and the California Institute of Technology. Keck time has been granted by NOAO (A285Hr).
[9] NSF Fellow.

Table 1
Candidates from HATNet Field G205

Star	R.A. (2000) Decl.	V	PM	$J - K_s$	P	Epoch (HJD)
HTR205-001	22:35:31.8 +39:53:59	11.03	12.1	0.08	1.25	...
HTR205-002	22:37:12.3 +38:13:43	10.06	8.52	0.63	2.44	...
HTR205-003	22:37:36.4 +34:36:24	12.48	24.7	0.33	2.17925 ± 0.00025	24452950.3206
HTR205-004	22:37:39.5 +38:07:43	12.22	27.6	0.42	5.45498 ± 0.00045	24452950.0516
HTR205-005	22:40:06.2 +37:31:39	11.88	5.81	0.39	4.35	...
HTR205-006	22:40:59.5 +35:25:22	11.82	1.07	0.76	3.61	...
HTR205-007W	22:44:02.4 +40:05:11	12.08	33.0	0.35	1.88249 ± 0.00032	24452911.5222
HTR205-007E	22:44:02.6 +40:05:11	11.50	33.0	0.35	1.88249 ± 0.00032	24452911.5222
HTR205-008	22:44:49.4 +39:28:50	10.61	10.6	0.78	1.63	...
HTR205-009	22:54:56.5 +34:31:42	10.93	6.04	0.27	1.55845 ± 0.00018	24452911.4381
HTR205-010	22:56:01.7 +37:51:06	11.33	7.02	0.31	2.51441 ± 0.00041	24452912.8156
HTR205-011	23:01:47.4 +38:06:22	11.19	13.1	0.38	3.13933 ± 0.00029	24452914.2476
HTR205-012	23:06:23.6 +39:07:19	12.28	18.4	0.35	3.15930 ± 0.00060	24452910.9429
HTR205-013	23:08:08.3 +33:38:03	10.72	24.7	0.28	2.23074 ± 0.00026	24452912.7566
HTR205-014	23:09:09.5 +36:40:38	10.28	10.7	0.13	7.20626 ± 0.00071	24452916.2177
HTR205-015	23:12:13.3 +37:44:09	11.11	11.1	0.64	1.192870 ± 0.000090	24452910.9437
HTR205-016	22:53:11.2 +34:44:41	11.21	10.1	0.81	1.56	...
HTR205-017	22:41:32.2 +36:36:22	11.94	2.76	0.32	4.79886 ± 0.00055	24452914.8199
HTR205-018	22:48:21.8 +35:54:53	11.71	26.9	0.35	0.55315 ± 0.00003	24452910.8027
HTR205-019	22:57:54.9 +33:39:00	11.47	9.79	0.61	5.14	...
HTR205-020	22:41:46.7 +36:49:28	10.57	7.43	0.09	6.52295 ± 0.00082	24452913.7491
HTR205-021	22:36:08.1 +37:50:26	10.27	86.1	0.40	0.789765 ± 0.000039	24452950.0783
HTR205-022	22:57:45.9 +38:40:26	10.00	49.5	0.27	4.46541 ± 0.00046	24452912.7253
HTR205-023	22:57:46.8 +38:40:29	10.40	...	0.30	4.46543 ± 0.00049	24453997.7926
HTR205-024	22:52:09.8 +35:26:49	10.17	76.0	0.26	3.07632 ± 0.00045	24454437.6758
HTR205-025	22:36:44.5 +40:03:13	10.93	2.2	0.78	6.39	...
HTR205-026	22:36:45.1 +35:08:06	12.09	20.5	0.36	3.73	...
HTR205-027	22:42:07.5 +39:02:43	13.63	58	0.89	0.555000 ± 0.000012	24452950.0867
HTR205-028	22:45:51.6 +40:28:37	13.92	12.4	0.63	1.56	...
HTR205-029	23:10:07.1 +41:05:11	13.51	...	0.39	3.72630 ± 0.00039	24453598.0809
HTR205-030	22:41:46.2 +37:13:43	12.39	33.7	0.39	1.60	...
HTR205-031	23:06:52.7 +34:21:24	13.02	1.2	0.29	0.750731 ± 0.000051	24452910.9452

Notes. Col. (1): HATNet transiting-planet candidate designation, Col. (2): right ascension and Declination from HATNet, Col. (3): estimated V magnitude, Col. (4): proper motion (mas yr^{-1}), Col. (5): $J - K_s$ color from 2MASS, Col. (6): photometric period (days), Col. (7): epoch of mid transit (Heliocentric Julian Day).

At the time of the early reduction of HATNet frames and the initial search for planet candidates, starting in the fall of 2003, our tools and strategies were much less developed than now. Although the Box Least Squares (BLS; Kovács et al. 2002) algorithm was already in routine use to search for periodic transit-like dips, the light curves themselves were still plagued by a variety of subtle trends. Some of these trends were not understood, and our intense effort to suppress them led to the development of the Trend Filtering Algorithm (TFA; Kovács et al. 2005). Later we gained a better understanding of the trends, and some were associated with "external parameters," such as sub-pixel position, airmass, stellar profile parameters, and the topology of other objects around the selected star. This led to the development of the External Parameter Decorrelation technique (EPD; Bakos et al. 2009), whereby we first correct for trends that have known underlying parameters. The EPD corrected light curves are then processed with TFA.

In the early reductions, these tools were simply not available. Thus, a variety of effects such as subtle out-of-transit (OOT) variations or color-dependent trends with atmospheric extinction went unrecognized or uncorrected, leading to (1) undetected shallow transits and (2) false alarms due to remaining trends. Furthermore, we were anxious to confirm our first HATNet transiting planet, and there was a strong temptation to retain as many candidates as possible for follow-up observations, including some where the detection of transit events was marginal. Field "G205" reductions witnessed all these changes, and the resulting candidate list is thus somewhat inhomogeneous.

The current pipeline, using multi-aperture photometry, EPD, TFA, and careful multi-step selection procedures, allows us to detect transit events for fainter stars. In addition, our rate of photometric false alarms has declined, due to both the improved photometry and several years of additional experience in how to evaluate the reliability of a possible detection.

Periodic transit-like dips in brightness were initially identified for 31 HATNet targets in field G205. These candidates are listed in Table 1. The periods that are given to two decimal places are from the original analysis of the light curves for periodic transits, while the periods that are accompanied by errors and epochs are from a reanalysis using the most recent tools. In the original photometric reduction of the HATNet G205 field, HTR205-001 yielded a light curve and was also identified as a planet candidate. The standard photometric reduction now relies on astrometry from Two Micron All Sky Survey (2MASS; Skrutskie et al. 2006). HTR205-001 is flagged as having poor quality in 2MASS, and therefore it was not included in the most recent photometric reduction. For 10 of the original candidates (HTR205-002, HTR205-005, HTR205-006, HTR205-008, HTR205-016, HTR205-019, HTR205-025, HTR205-026, HTR205-028, and HTR205-030), the latest reductions and analysis no longer yield reliable periods. They are now considered photometric false alarms

and are also listed with their original periods to two decimal places. For six of the candidates (HTR205-004, HTR205-010, HTR205-011, HTR205-012, HTR205-017, and HTR205-020), the periods listed in Table 1 have been doubled from the values yielded by the most recent analysis of the light curves in order to closely match the periods yielded by the spectroscopic orbits reported in this paper. The ephemerides listed for HTR205-023 and HTR205-024 are taken from Winn et al. (2007) and from the solution reported later in this paper, respectively.

One of the initial candidates, HTR205-007, turned out to be a close pair of stars separated by only 3.″2, so it is listed as two candidates in Table 1, HTR205-007E and HTR205-007W. The photometry of another one of the initial candidates, HTR205-018, turned out to be contaminated by the light of a nearby eclipsing system. This problem was revealed by an additional step in the photometric analysis, which is now applied routinely to all candidates. To explore the possibility that a transiting-planet candidate is a blend with a nearby variable, we now inspect the light curves of all the stars within about 1′ of the candidate and brighter than $I = 14$ mag. In the case of HTR205-018, a star separated by 22″ from HTR205-018 (at $\alpha = 22^{\rm h}48^{\rm m}23\overset{\rm s}{.}4$, $\delta = +35^\circ55'5''$) and approximately 1.2 mag fainter in the HATNet band showed events with the same ephemeris, but with a depth of 0.0199 mag compared to 0.007 mag for HTR205-018. Correcting for the dilution by the contaminating light from HTR205-018, the actual depth works out to about 0.05 mag. This is too deep to be a transiting planet around HTR205-018, if it is a Sun-like star as implied by its $J - K = 0.35$ color index, so both the companion and HTR205-018 were withdrawn as viable candidates.

In a previous publication (Bakos et al. 2007a), HTR205-023 was announced as HAT-P-1b, the first confirmed transiting planet from HATNet. In this paper, we confirm that a second candidate in field G205, HTR205-024, is also a transiting planet, which we designate HAT-P-8b.

3. FOLLOW-UP OBSERVATIONS

Our strategy for following up transiting-planet candidates identified by wide-angle ground-based photometric surveys such as HATNet involves both spectroscopy and photometry. The discovery light curves from small cameras such as those used by HATNet rarely provide the photometric precision and time resolution needed for accurate determinations of planetary radii. On the other hand, large-format CCD cameras on wide-field meter-class telescopes are well suited for obtaining high-quality light curves for candidates identified by wide-angle surveys such as HATNet. For the photometric follow up of many of the most interesting candidates identified by HATNet, we have used KeplerCam on the 1.2 m reflector at FLWO. KeplerCam uses a 4K×4K Fairchild 486 CCD with 0.″33 pixels, 23′ field of view, and camera overhead of 12 s for 2 × 2 binning.

However, photometric observations with KeplerCam are not usually the first step in the follow up of a HATNet candidate, for the simple reason that observations during transit occupy only a few percent of the time and are difficult to schedule. Instead our usual strategy has been to start with a spectroscopic reconnaissance, to look for orbital motion due to a stellar companion and to better characterize the target. These observations are much easier to schedule, because the radial velocity varies continuously throughout an orbit.

For the reconnaissance spectroscopy, we have been using the CfA Digital Speedometers (Latham 1992), mostly on the 1.5 m Tillinghast Reflector at FLWO, but also on the 1.5 m Wyeth Reflector at the Oak Ridge Observatory in the Town of Harvard, MA, up until 2005 when that facility was terminated. These venerable instruments use intensified photon-counting Reticon detectors on identical echelle spectrographs to record 45 Å of spectrum centered at 5187 Å, thus including the gravity-sensitive Mg b features. Our usual strategy for follow up of a new candidate has been to obtain an initial spectrum. If it shows decent lines we then get a second spectrum, the next night if possible, so that we can check to see if the velocity varies. For slowly rotating solar-type stars, the typical velocity precision is 0.5 km s^{-1}, which is adequate for the detection of a companion down to a limit of about 10 $M_{\rm J}$ for periods of a few days. Stellar companions induce much larger orbital amplitudes and are easy to identify if there are only two objects in the system.

The same spectra that are used to determine velocities are also used to characterize the effective temperature, surface gravity, and projected rotational velocity of the host star, using an extensive library of synthetic spectra to find the template spectrum that gives the best match to the observed spectra, based on grids of one-dimensional correlations. Because of the narrow wavelength range of these spectra, there is a degeneracy between temperature, gravity, and metallicity. For solar-type stars, a lower metallicity results in a spectrum that looks hotter and/or has a weaker surface gravity. Thus, for the initial characterization we assume solar metallicity. This allows us to determine the astrophysical parameters with a typical precision of 150 K for effective temperature, 1 dex for log surface gravity, and 1 km s^{-1} for the projected rotational velocity, although the rotation becomes more sensitive to systematic errors for stars rotating more slowly than the instrumental resolution of 8.5 km s^{-1}, and is not reliable for stars rotating more rapidly than about 120 km s^{-1}. The rotation is relatively insensitive to the temperature, gravity, and metallicity. However, the temperature and gravity may have systematic errors that are several times larger than the precisions quoted above if the metallicity is substantially different from solar. As a rough rule of thumb, for solar-type stars a decrease in the metallicity of 0.5 dex must be compensated by a decrease in the temperature of about 200 K in order to retain the observed line strengths.

The strategy of most wide-angle ground-based photometric surveys for transiting planets, including HATNet, is to analyze every point source down to some limiting magnitude whose value is set by the desired photometric performance. Thus, many of the HATNet candidates prove to be evolved. If the surface gravity that we derive from the CfA spectra is weaker than $\log g = 3.25$ and there is no significant rotation, we assume that the primary star is a giant diluting the light of an eclipsing binary that is unresolved in the HATNet images, either a physically bound system or a chance alignment. Normally, we put aside the targets classified as giants and do not invest additional resources in follow-up observations.

If the CfA spectra indicate that a candidate has a temperature and gravity consistent with a star on or near the main sequence and the initial spectra show no velocity variations, we usually schedule additional observations the next month to make sure the velocity does not vary. If the candidate survives this stage, only then do we try to schedule photometric observations with KeplerCam, with the goal of determining a high-quality light curve for a transit event. However, this step is not practical if the photometric ephemeris is not accurate enough to predict the time of transit within a few hours. The failure to confirm a transit with high-quality photometry is ambiguous,

and cannot distinguish a photometric false alarm from an inadequate ephemeris. Confirmation that a candidate undergoes transits is an area where smaller telescopes can contribute, such as sophisticated facilities operated by amateurs (McCullough et al. 2006) or the network of photometric telescopes planned for the Las Cumbres Observatory Global Telescope Network (Brown et al. 2007).

Because the HATNet pixels are so large on the sky (about 14″ for the original 2K×2K CCDs used to observe field G205 and 9″ for the 4K×4K CCDs now in use), many of the candidates prove to have close companions when viewed with much higher spatial resolution. In some cases, this allows us to use KeplerCam to demonstrate that the transit-like light curve is actually due to a nearby eclipsing binary diluted by the brighter target star.

Candidates that show no velocity variation at the level of a few hundred m s^{-1} with the reconnaissance spectroscopy and have a good-quality light curve consistent with a transiting planet are then followed up for very precise velocities with facilities such as HIRES on Keck I, HRS on Subaru, and/or Sophie at the Haute Provence Observatory, in order to derive orbital solutions for the host star and thus the mass of the planet relative to the host star.

3.1. Reconnaissance Spectroscopy

Starting in 2004 January, all but 4 of the 32 transiting-planet candidates identified in HATNet field G205 were observed with the CfA Digital Speedometers (Latham 1992). The remaining four are faint and have not yet been observed. Of those observed, all but one yielded reliable radial velocities, as described below. The only one for which we were unable to determine a velocity was HTR205-014, whose spectrum proved to be featureless in the Mg b region. In retrospect, this result is not surprising, given this star's very hot 2MASS color, $J - K_s = 0.13$ mag. In the early days, when we were anxious to confirm our first HATNet transiting planet, we followed up everything that looked like it might be a planet, no matter what its color or proper motion. The 2MASS colors from the near infrared are relatively insensitive to reddening and thus provide a good initial guess for the temperature of a star. Moreover, the 2MASS spatial resolution is much better than the HATNet cameras, and 2MASS can be used to track down nearby companions that contaminate the HATNet images. Finally, the 2MASS astrometry is of reliably high quality and is quite useful in the reduction and analysis of images.

The radial velocities of the 27 candidates in field G205 with reliable measurements are reported for all the individual observations in Tables 2 and 3. The velocity results for the 19 stars in Table 2 are based on one-dimensional correlations using **rvsao** running inside IRAF[10] and templates from our library of synthetic spectra calculated by Jon Morse (e.g., see Latham et al. 2002). For four of the targets (HTR205-004, HTR205-010, HTR205-011, and HTR205-020), the double-lined nature of the spectra was obvious from the one-dimensional correlation analysis of the first two exposures, and the velocities for both components of these binaries are listed in Table 3 based on two-dimensional correlations using TODCOR (Zucker & Mazeh 1994) as implemented at CfA by GT. Eventually, it was possible to use TODCOR to dig out secondary velocities for two additional binaries (HTR205-012 and HTR205-017), once single-lined orbital solutions were available and could be used to guide the search for the secondary correlation peaks.

[10] IRAF (Image Reduction and Analysis Facility) is distributed by the National Optical Astronomy Observatories, which is operated by the Association of Universities for Research in Astronomy, Inc., under cooperative agreement with the National Science Foundation.

Table 2
Single-lined Radial Velocities

Star	Tel	Template	HJD	V_A	$\sigma(V_A)$
HTR205-001	T	t10000g45p00v008	2453158.90513	−2.58	0.65
HTR205-001	T	t10000g45p00v008	2453161.96505	−2.75	0.58
HTR205-001	W	t10000g45p00v008	2453183.82621	−2.19	1.17
HTR205-002	W	t05000g30p00v000	2453137.83494	−27.03	0.27
HTR205-002	W	t05000g30p00v000	2453154.80255	−27.06	0.28
HTR205-002	W	t05000g30p00v000	2453180.82534	−26.76	0.26
HTR205-003	T	t06500g45p00v030	2453162.91121	−23.55	1.27
HTR205-003	T	t06500g45p00v030	2453183.95068	−67.55	1.48
HTR205-003	T	t06500g45p00v030	2453511.95989	−1.53	2.43

Notes. Col. (1): HATNet transiting-planet candidate designation, Col. (2): telescope (W = Wyeth, T = Tillinghast), Col. (3): template parameters encoded in the form tTTTTTgGGp00vVVV, where TTTTT gives the effective temperature in K, GG the log surface gravity times 10 in cgs units, p00 signifies that the metallicity [m/H] is plus 0, i.e., solar, and VVV is the rotational velocity in km s^{-1}, Col. (4): Heliocentric Julian Date, Col. (5): heliocentric radial velocity (km s^{-1}), Col. (6): radial velocity error estimate (km s^{-1}).

(This table is available in its entirety in a machine-readable form in the online journal. A portion is shown here for guidance regarding its form and content.)

In the case of the spectra analyzed with TODCOR, the choice of primary template was based on grids of one-dimensional correlations, while the choice of secondary template used the results of the orbital solution for guidance.

The mean velocities and various indicators of the uncertainties are presented in Table 4. For those binaries with orbital solutions, the mean velocity and error are actually the center-of-mass velocity and error estimate from the orbital solution. Otherwise the error of the mean velocity is one of the following two, whichever is larger: the actual observed rms velocity residuals divided by the square root of the number of observations, or the average of the internal velocity error estimates, again divided by root N_{obs}. $P(\chi^2)$ is the probability of observing velocity residuals and corresponding χ^2 larger than the actual observed residuals and χ^2, assuming a star with constant velocity and Gaussian errors for the observed velocities. Experience shows that stars with $P(\chi^2)$ values less than 0.001 usually prove to be binaries. For 10 of the candidates, the radial velocity data were sufficient to allow orbital solutions. The orbital parameters are reported in Tables 5 and 6.

3.1.1. Spectroscopic Binaries with Orbital Solutions

Ten of the candidates with variable velocities yielded orbital solutions. For eight of these (see Figure 1: HTR205-003, HTR205-004, HTR205-010, HTR205-011, HTR205-012, HTR205-013, HTR205-017, and HTR205-020), the orbital period is consistent with the photometric period from HATNet within the errors. This agreement proves beyond a reasonable doubt that the observed light curves are actually due to eclipses by stellar companions. Note that for six of these binaries, the orbital period is actually twice the original HATNet photometric period. When the primary and secondary eclipses are not very different and the orbit is circular, the analysis of the photometry for periodic events often settles on half the true period. This implies that the eclipses must be grazing, in order to produce the small observed dips. The two exceptions are the eclipsing binaries HTR205-003 and HTR205-013, where the companions are M dwarfs and the secondary eclipse is much too weak for detection with HATNet, despite the fact that the eclipses are full.

Table 3
Double-lined Radial Velocities

Star	Template A	Template B	HJD	V_A	V_B
HTR205-004	t06250g40p00v016	t06250g40p00v016	24453162.9343	−41.09	−16.87
HTR205-004	t06250g40p00v016	t06250g40p00v016	24453183.9643	22.52	−83.60
HTR205-004	t06250g40p00v016	t06250g40p00v016	24453188.9069	45.65	−102.90
HTR205-004	t06250g40p00v016	t06250g40p00v016	24453684.6943	37.57	−102.34
HTR205-004	t06250g40p00v016	t06250g40p00v016	24453689.6640	5.36	−72.24
HTR205-004	t06250g40p00v016	t06250g40p00v016	24453694.6542	−23.91	−36.67
HTR205-004	t06250g40p00v016	t06250g40p00v016	24453714.6282	−97.31	39.29
HTR205-004	t06250g40p00v016	t06250g40p00v016	24453746.5850	−41.46	−19.67
HTR205-004	t06250g40p00v016	t06250g40p00v016	24453984.8431	42.79	−102.59

Notes. Col. (1): HATNet transiting-planet candidate designation, Col. (3): template for primary, Col. (3): template for secondary, Col. (4): Heliocentric Julian Date, Col. (5): primary heliocentric radial velocity (km s^{-1}), Col. (6): secondary heliocentric radial velocity (km s^{-1}).

(This table is available in its entirety in a machine-readable form in the online journal. A portion is shown here for guidance regarding its form and content.)

Table 4
Mean Radial Velocities and Error Estimates

Star	N_{obs}	Span	$\langle V_{rot}\rangle$	$\langle V_{rad}\rangle$	±	Ext	Int	E/I	χ^2	P(χ^2)	$\langle ht\rangle$	Comments
HTR205-001	3	24	8.0	−2.48	0.48	0.36	0.83	0.43	0.35	0.838	0.64	P?
HTR205-002	3	43	0.5	−26.96	0.21	0.16	0.37	0.44	0.40	0.820	0.93	G,WD
HTR205-003	17	879	31.0	−34.96	0.49	1.77	1.88	0.94	...	...	0.68	EB,SO
HTR205-004	12	882	17.3	−30.92	0.53	3.06	2.10	1.45	...	...	...	EB,DO
HTR205-005	2	25	60.2	−16.17	26.8	37.9	6.18	6.14	52.48	0.000	0.21	S,FR,WD
HTR205-006	2	504	0.0	−51.40	0.37	0.53	0.38	1.39	1.93	0.165	0.91	G,WD
HTR205-007W	4	793	53.0	−17.44	15.32	30.63	2.67	11.45	508.86	0.000	0.54	S,FR
HTR205-007E	2	2	7.4	−36.25	0.73	1.04	0.80	1.29	1.68	0.712	0.71	P?
HTR205-008	3	22	3.0	+31.65	0.22	0.22	0.39	0.57	0.62	0.733	0.91	G,WD
HTR205-009	1	0	120	+2.50	5.16	...	5.16	...	...	...	0.34	FR
HTR205-010	11	362	45.8	−11.67	0.78	2.44	3.83	0.64	...	...	0.56	EB,DO
HTR205-011	11	804	22.1	−6.22	0.39	2.01	4.43	0.45	...	...	0.64	EB,DO
HTR205-012	13	832	36.0	−30.75	0.73	3.16	2.75	1.15	...	...	0.57	EB,DO
HTR205-013	23	630	28.9	−9.74	0.23	1.01	1.24	0.82	...	...	0.80	EB,SO
HTR205-014	2	31	...	...	...	...	...	...	...	...	...	FR
HTR205-015	2	386	3.0	−42.64	0.35	0.26	0.50	0.53	0.30	0.587	0.88	G
HTR205-016	3	504	0.0	−30.05	0.25	0.22	0.44	0.49	0.53	0.765	0.88	G,WD
HTR205-017	12	804	10.6	−9.03	0.31	0.94	0.76	1.23	...	...	0.73	EB,DO
HTR205-018	5	114	5.9	−23.07	0.23	0.28	0.52	0.54	1.50	0.826	0.86	NEB
HTR205-019	10	862	0.0	−38.85	0.20	0.31	0.44	0.71	0.71	...	0.89	G,SO,WD
HTR205-020	10	804	13.1	−12.26	0.30	0.97	1.33	0.73	...	...	0.49	EB,DO
HTR205-021	12	919	0.5	−6.86	0.11	0.21	0.48	0.44	...	...	0.88	SO
HTR205-022	6	233	7.5	−3.44	0.19	0.32	0.47	0.68	2.02	0.846	0.88	NP
HTR205-023	6	233	1.5	−2.94	0.23	0.55	0.49	1.14	6.19	0.288	0.88	P
HTR205-024	8	357	12.8	−22.53	0.28	0.79	0.64	1.23	10.23	0.176	0.85	P
HTR205-025	2	4	0.8	−42.63	0.27	0.27	0.38	0.71	0.50	0.478	0.92	G,WD
HTR205-026	4	293	0.5	−17.49	0.26	0.34	0.51	0.66	1.09	0.780	0.82	WD
HTR205-027	0											
HTR205-028	0											
HTR205-029	0											
HTR205-030	4	214	3.4	−23.67	0.45	0.90	0.59	1.52	7.44	0.059	0.823	WD
HTR205-031	0											

Notes. Col. (1): HATNet transiting-planet candidate designation, Cols. (2) and (3): number of observations and time spanned (days), Col. (4): projected rotational velocity for the primary derived from one-dimensional correlations (km s^{-1}), Col. (5): mean radial velocity or center-of-mass velocity from an orbital solution (km s^{-1}), Col. (6): error in the mean velocity (km s^{-1}), Col. (7): external rms residuals in the observed velocities of the primary; from the orbital fit in the case of a binary (km s^{-1}), Col. (8): mean internal velocity error estimate (km s^{-1}), Col. (9): ratio of external to internal errors, Cols. (10) and (11): χ^2 and χ^2 probability, Col. (12): mean of the peak correlation height, Col. (13): Comments: DO = double-lined orbital solution, EB = eclipsing binary, FR = rapidly rotating star, G = giant, NEB = blend with nearby eclipsing binary, NP = blend with nearby transiting planet, S = velocity is variable, SO = single-lined orbital solution, P = planet confirmed by a solution for the spectroscopic orbit, P?=possible transiting planet, WD = withdrawn by HATNet as a photometric false alarm.

A detailed analysis of HTR205-013 has already been published by Beatty et al. (2007).

For all eight of the confirmed eclipsing binaries, the orbital solutions yield eccentricities which are indistinguishable from zero when the eccentricity is allowed to be a free parameter in the solution (see Table 7), presumably because the orbits have been circularized by tidal mechanisms. Thus for the final orbital solutions we adopted $e \equiv 0$, and the epochs for these binaries

Table 5
Single-lined Orbital Solutions

Star	P	γ	K	e	ω	T	$a_A \sin i$	$f(m)$	N σ	Span Cycles
HTR205-003	2.178207	−34.96	34.84	0.0	...	53599.1750	1.044	0.0096	17	879.8
	±0.000069	±0.49	±0.60	...	...	±0.0071	±0.075	±0.0021	1.77	403.7
HTR205-013	2.230716	−9.74	18.42	0.0	...	53197.72708	0.565	0.00144	23	630.2
	±0.000049	±0.23	±0.31	...	...	±0.00022	±0.029	±0.00022	1.01	282.5
HTR205-019	94.331	−38.85	25.48	0.408	289.1	53738.53	30.17	0.1230	10	862.7
	±0.035	±0.20	±0.33	±0.010	±1.4	±0.21	±0.18	±0.0022	0.31	9.1
HTR205-021	113.301	−6.86	20.85	0.364	238.2	53653.53	30.248	0.08591	12	919.6
	±0.056	±0.011	±0.12	±0.006	±1.1	±0.23	±0.058	±0.00052	0.21	8.1

Notes. Col. (1): HATNet transiting-planet candidate designation, Col. (2): period P in days, Col. (3): center-of-mass velocity γ in km s^{-1}, Col. (4): projected orbital semi-amplitude of the primary K in km s^{-1}, Col. (5): eccentricity e, assumed circular if no error, Col. (6): angle of periastron ω in degrees, Col. (7): Heliocentric Julian Date −2,400,000 for periastron passage T, or for maximum velocity if $e = 0$ is assumed, Col. (8): projected semimajor axes of the primary $a \sin i$ in Gm, Col. (9): mass function $f(m)$ in $M_\odot$, Col. (10): number of velocities and rms velocity residuals in km s^{-1}, Col. (11): time spanned by the observations in days and number of orbital cycles covered.

Table 6
Double-lined Orbital Solutions

Star	P q	γ	K_A K_B	T	$a_A \sin i$ $a_B \sin i$	$M_A \sin^3 i$ $M_B \sin^3 i$	N σ	Span Cycles
HTR205-004	5.45504	−30.92	77.3	53633.0976	5.80	1.067	12	882.8
	±0.00014	±0.53	±1.4	±0.0077	±0.12	±0.035	3.1	181.8
	0.989	...	78.2	...	5.86	1.056	12	...
	±0.024	...	±1.0	...	±0.08	±0.044	2.0	...
HTR205-010	2.514414	−11.67	95.9	53876.8713	3.316	1.23	11	362.9
	±0.000082	±0.78	±1.2	±0.0048	±0.048	±0.10	2.4	144.3
	0.866	...	110.7	...	3.83	1.067	11	...
	±0.036	...	±3.8	...	±0.15	±0.054	8.8	...
HTR205-011	3.139408	−6.22	92.0	53715.7397	3.973	1.049	11	804.9
	±0.000047	±0.39	±1.2	±0.0026	±0.057	±0.026	2.0	256.4
	0.983	...	93.6	...	4.041	1.032	11	...
	±0.018	...	±0.9	...	±0.043	±0.031	1.5	...
HTR205-012	3.159326	−30.75	83.5	53683.3584	3.627	1.137	13	832.8
	±0.000058	±0.73	±1.3	±0.0056	±0.064	±0.052	3.2	263.6
	0.823	...	101.5	...	4.409	0.935	13	...
	±0.021	...	±1.8	...	±0.089	±0.038	4.4	...
HTR205-017	4.802778	−9.03	67.25	53678.3002	4.441	1.27	12	803.9
	±0.000096	±0.31	±0.43	±0.0051	±0.032	±0.14	0.9	167.4
	0.701	...	95.9	...	6.33	0.890	12	...
	±0.036	...	±4.2	...	±0.31	±0.052	10.8	...
HTR205-020	6.52289	−12.26	63.16	53703.7368	5.664	2.128	10	804.0
	±0.00015	±0.30	±0.30	±0.0065	±0.043	±0.059	1.0	123.3
	0.586	...	107.7	...	9.67	1.247	10	...
	±0.008	...	±1.1	...	±0.12	±0.025	2.7	...

Notes. Col. (1): HATNet transiting-planet candidate designation, Col. (2): period P in days, Col. (3): center-of-mass velocity γ in km s^{-1}, Col. (4): projected orbital velocities of the primary and secondary K_A and K_B in km s^{-1}, Col. (5): Heliocentric Julian Date −2,400,000 for time of maximum velocity T, Col. (6): projected semimajor axes of the primary and secondary $a_A \sin i$ and $a_B \sin i$ in Gm, Col. (7): projected masses of the primary and secondary $M_A \sin^3 i$ and $M_B \sin^3 i$ in $M_\odot$, Col. (8): number of velocities and rms velocity residuals in km s^{-1} for the primary and secondary, and Col. (9): time spanned by the observations in days and number of orbital cycles covered.

listed in Tables 5 and 6 are the times of maximum velocity rather than the times of periastron passage.

The preliminary orbital solutions presented here and the HATNet discovery light curves are not good enough to justify full-blown analyses of the confirmed eclipsing binaries. However, some of these systems may merit further investigation. To provide some guidance for such efforts, we summarize some of the expected characteristics of these binaries in Table 8. As an estimate of the mass of each primary in a double-lined system, we list the minimum mass from the orbital solution. This is the same as the actual mass if the orbit is viewed exactly edge-on. To estimate the radius of the primary, we invoke the broadening of the lines that we derive from the CfA spectra. Tidal mechanisms tend to align the stellar rotation axes with the orbital axis, to synchronize the rotational periods with the orbital period, and to circularize the orbit, normally with the sequence of events in this order (e.g., see Zahn 1989). Because all of our eclipsing binaries show circular orbits, we can reasonably assume that the rotation of the stars has been synchronized and aligned with the orbit, and thus we can use the projected rotational velocity,

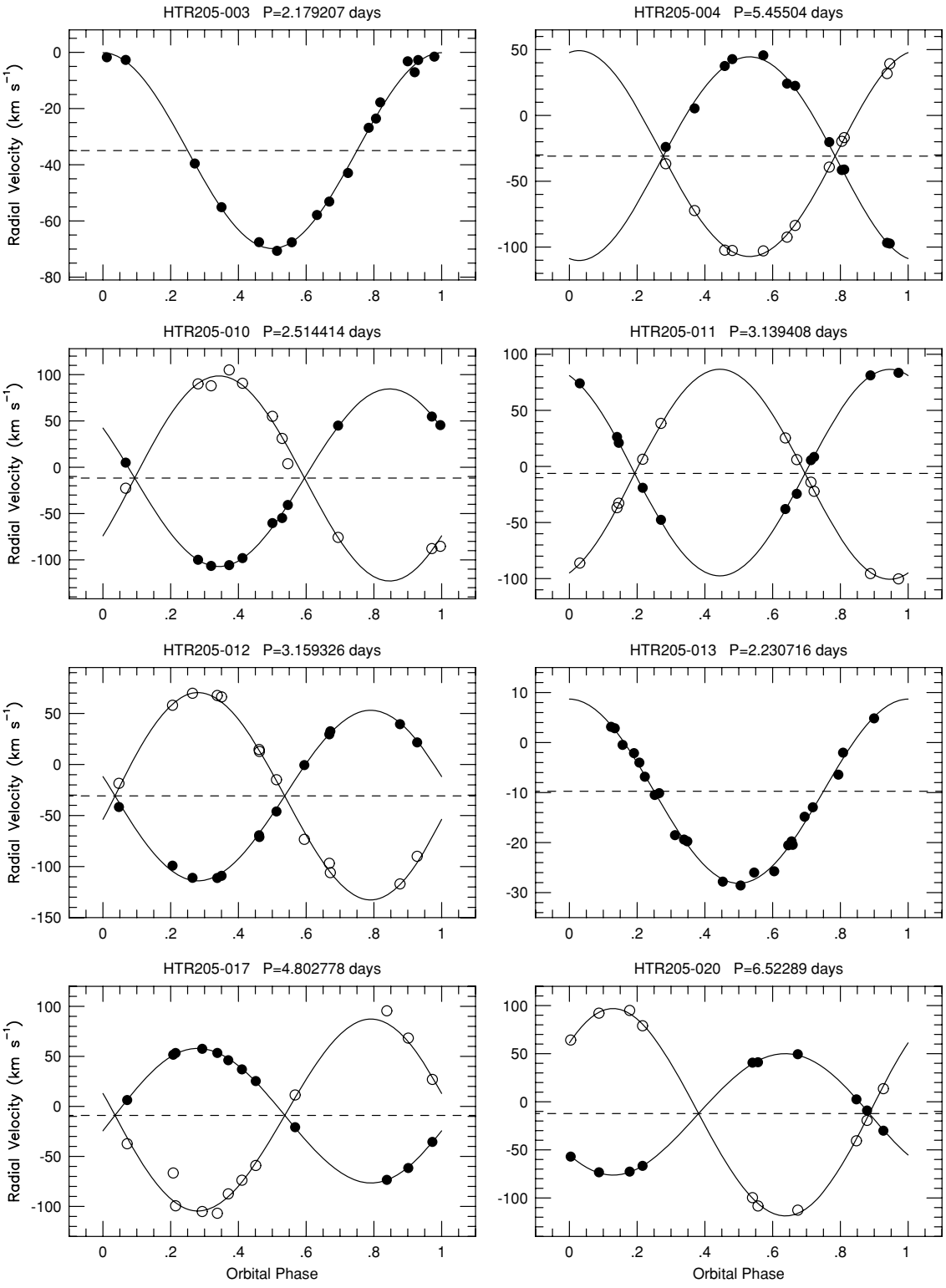

Figure 1. Velocity curves for the eight confirmed eclipsing binaries, phased to the orbital solution reported in Tables 5 and 6, together with the observed velocities.

$v \sin i_{\rm rot}$, to estimate the radius of the primary, $R_{\rm A}$:

$$R_{\rm A} = 0.0198(v \sin i_{\rm rot}) P_{\rm rot} / \sin i_{\rm rot}, \quad (1)$$

where $P_{\rm rot} \equiv P_{\rm orb}$ and $i_{\rm rot} \equiv i_{\rm orb}$ by assumption, and the coefficient 0.0198 delivers the radius in solar units if the rotational broadening is in km s^{-1} and the period is in days.

For 2 of the 10 spectroscopic binaries with orbital solutions (plotted in Figure 2; HTR205-019 and HTR205-021), the orbital period is much longer than the photometric period from HATNet. Thus, the stellar companions responsible for the orbital motion cannot be responsible for the observed dips in the HATNet light curves for these candidates. A possible explanation is that the light of the observed primary is diluting the light from a nearby eclipsing binary that is not spatially resolved by HATNet, either in a physical system or a chance alignment. If the eclipsing binary is bound to the primary,

Table 7
Orbital Eccentricities

Star	e	$\sigma(e)$
HTR205-003	0.025	±0.020
HTR205-004	0.025	±0.011
HTR205-010	0.007	±0.016
HTR205-011	0.0085	±0.0065
HTR205-012	0.000	±0.011
HTR205-013	0.012	±0.021
HTR205-017	0.0318	±0.0055
HTR205-019	0.408	±0.010
HTR205-020	0.0191	±0.0074
HTR205-021	0.364	±0.006

Notes. Col. (1): HATNet transiting-planet candidate designation, Col. (2): orbital eccentricity e when allowed to be a free parameter, Col. (3): estimated standard deviation of e.

then the orbital motion observed for the primary may reflect its orbit around the eclipsing binary, in which case only three stars are needed to explain the observations. If the separation between the primary and the eclipsing binary is very wide, either in a long-period orbit or because the alignment is due to chance, then four stars are required to explain the observations. Support for the interpretation that an observed HATNet light curve arises from a diluted eclipsing binary can come from a better light curve observed with a larger telescope. Higher spatial resolution may reveal that a nearby eclipsing binary was blended with the target in the HATNet images and is the source of the transit-like event. Even if the eclipsing binary is not resolved spatially, better photometric precision may be able to show that the ingress and egress last longer than allowed by the observed eclipse depth, thus indicating that the eclipsing objects are larger than implied by the depth because of dilution by the primary star. Another possible explanation is that the HATNet detection is a photometric false alarm. This possibility could also be checked by obtaining high-quality light curves. However, a failure to confirm an event predicted by the HATNet photometric ephemeris may be inconclusive if the ephemeris is not accurate enough, which often happens when considerable time has elapsed between the HATNet observations and the follow-up work.

3.1.2. Evolved Primaries

For seven of the candidates (HTR205-002, HTR205-006, HTR205-008, HTR205-015, HTR205-016, HTR205-019, and HTR205-025), our analysis of the CfA spectra implies that the primary star is evolved ($\log g = 3.25$ or weaker). In all seven cases the available proper motions are small, supporting the interpretation that the targets are distant and therefore intrinsically luminous. Of course, a small proper motion is not proof that the distance to a star is large, because the space motion of the star may be mostly directed along the line of sight. Conversely, a large proper motion does not prove that the star is nearby, because metal-poor giants, although quite rare, can have very large space motions.

Main-sequence stars come in a wide range of sizes, so it is not hard to find a dwarf star with the right size to reproduce the observed eclipse depth for each of the seven giants. However, this explanation fails, because the photometric periods are all very short and would require that the companion orbit inside the giant. Thus, the possible explanations for the source of the dips in the light curves of these giants are the same as for the two long-period binaries discussed above (HTR205-019 and HTR205-021). Indeed, one of the seven giants is the primary in one of those binaries (HTR205-019), with an orbital period of 94 days.

Table 8
Eclipsing Binary Radii

Star	$v \sin i_{\rm rot}$	$P_{\rm rot}$	$R_{\rm A}$	$M_{\rm A} \sin^3 i$	q	$T_{\rm eff}$	$\log g$	$L_{\rm B}/L_{\rm A}$
HTR205-003	31.0	2.179	1.34	...	...	6500	4.5	...
HTR205-004	17.3	5.455	1.87	1.07	0.99	6250	4.0	1.00
HTR205-010	45.8	2.514	2.28	1.23	0.87	5750	3.5	0.36
HTR205-011	22.1	3.139	1.37	1.05	0.98	5500	3.5	0.90
HTR205-012	36.0	3.159	2.25	1.13	0.82	6250	4.0	0.24
HTR205-013	28.9	2.231	1.27	...	...	6250	4.0	...
HTR205-017	10.6	4.803	1.01	1.26	0.70	6750	4.0	0.09
HTR205-020	13.1	6.523	1.69	2.12	0.59	11500	5.0	0.09

Notes. Col. (1): HATNet transiting-planet candidate designation, Col. (2): spectroscopic projected rotational velocity $v \sin i_{\rm rot}$ in km s^{-1}, where the inclination of the rotational axis, $i_{\rm rot}$ is assumed to be the same as the inclination of the orbital axis, $i_{\rm orb}$, Col. (3): rotational period, $P_{\rm rot}$, assumed equal to the orbital period P, Col. (4): radius of the primary, $R_{\rm A}$, assuming synchronized and aligned rotation, Col. (5): minimum mass of the primary in a double-lined binary, $M_{\rm A} \sin^3 i$, Col. (6): secondary to primary mass ratio, $M_{\rm B}/M_{\rm A}$, Col. (7): spectroscopic effective temperature estimate for the primary, $T_{\rm eff}$, Col. (8): spectroscopic log surface gravity estimate for the primary, $\log g$, Col. (9): luminosity ratio at 5187 Å from TODCOR, $L_{\rm B}/L_{\rm A}$.

3.1.3. Rapid Rotators

For four of the candidates (HTR205-005, HTR205-007W, HTR205-009, and HTR205-014), the line broadening observed in the CfA spectra implies that the stars are rotating much too rapidly to allow radial velocities to be determined with enough precision to derive a spectroscopic orbit for a planetary companion. As mentioned above, the spectrum of HTR205-014 appears featureless in the Mg b region of the spectrum, and no reliable radial velocity could be determined from the CfA spectrum. In the other three cases our analysis did yield velocities, but with very large uncertainties. The rotation that we derived for HTR205-009 is 120 km s^{-1}, near the limit where the CfA velocities become unreliable. Therefore, we did not bother to get a second spectrum for this star. For HTR205-005 and HTR205-007W, we did obtain additional spectra. In both cases, the resulting velocities showed significant variation. Presumably both stars are spectroscopic binaries.

3.1.4. Stars with No CfA Velocity Variations

For seven of the unevolved stars, the CfA spectra yielded rotational velocities slower than 10 km s^{-1} and $P(\chi^2)$ values for the velocity residuals larger than 0.05, namely there was no evidence of velocity variations. Thus, these seven systems survived the initial reconnaissance spectroscopy and deserved further consideration as viable planet candidates. One of these seven is HTR205-001, which has a very blue 2MASS color of $J - K_{\rm s} = 0.08$ mag. Indeed the effective temperature derived from the CfA spectra proved to be uncomfortably hot, $T_{\rm eff} = 10{,}000$ K. Nevertheless, the rotation derived from the CfA spectra is quite modest, $v \sin i = 8$ km s^{-1}, and the three CfA velocities have an rms value of only 0.43 km s^{-1}. If the source of the observed dip in the light curve is a transiting planet, it would have to be enormously bloated. Although this candidate has not yet been absolutely ruled out as a transiting planet, so far we have not followed up with additional observations.

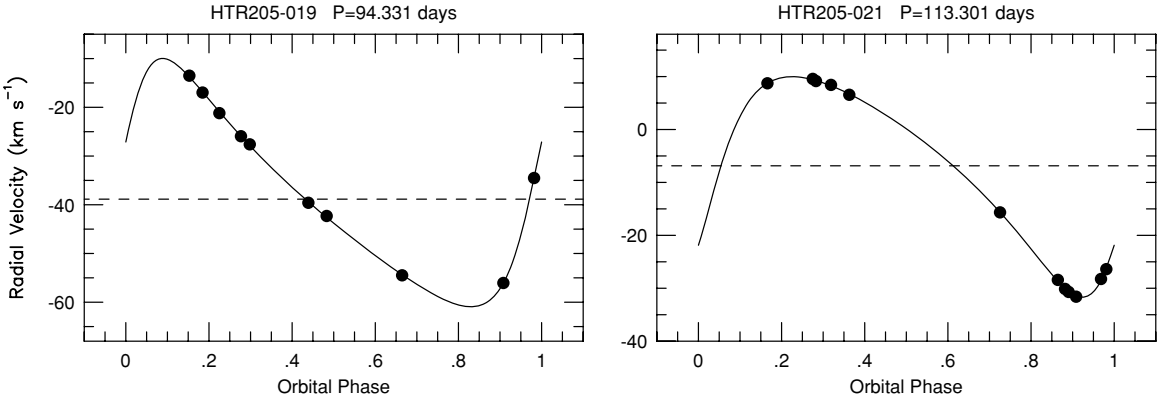

Figure 2. Velocity curves and observed velocities for the two single-lined binaries with orbital solutions reported in Table 5 that do not match the photometric ephemerides. In particular, the orbital periods are considerably longer than the photometric periods.

The eastern star in the close visual pair HTR205-007 also survives as a viable planet candidate. In this case, we have not pursued the candidate with additional observations, partly because of the difficulty in obtaining a high-quality light curve with KeplerCam for a pair of stars that are separated by only 3.″2. Furthermore, the fact that the nearby companion appears to be a spectroscopic binary with a large velocity amplitude and rapid rotation suggests that it is likely to be the source of the dip in the HATNet light curve.

Two of the surviving candidates, HTR205-026 and HTR205-030, were subsequently withdrawn as photometric false alarms, based on an independent reduction and analysis of their HATNet photometric time series with the most recent tools and procedures. It is interesting to note that the same reanalysis concluded that six of the candidates classified spectroscopically as giants (HTR205-002, HTR205-006, HTR205-008, HTR205-016, HTR205-019, and HTR205-025) were also photometric false alarms in the original analysis.

Both members of the visual pair HTR205-022 and HTR205-023 with separation 11.″2 showed similar velocities and no significant velocity variation based on the CfA spectra. Subsequent follow-up observations showed that HTR205-023 is the star hosting a transiting planet (Bakos et al. 2007b), not HTR205-022. The mean velocities and stellar parameters for the two stars are consistent with the interpretation that they are a bound physical pair.

In this paper, we report the confirmation of a planet transiting the final of these seven candidates, HTR205-024, which we designate HAT-P-8b.

4. HAT-P-8b

4.1. HATNet Photometry

In a previous publication (Bakos et al. 2007a), HTR205-023 was announced as the first confirmed transiting planet from the HATNet survey and was assigned the designation HAT-P-1b. In this paper, we confirm that a second candidate in field G205, HTR205-024, is also a transiting planet, which we designate HAT-P-8b. This target is the $I \approx 9.68$ mag star GSC 02757-01152 (also known as 2MASS 22520985+3526495; $\alpha = 22^{\rm h}52^{\rm m}09\overset{\rm s}{.}85$, $\delta = +35^\circ 26' 49\overset{''}{.}5$; J2000), with a transit depth of $\sim$ 7.0 mmag, a period of $P = 3.076$ days and a relative duration (first to last contact) of $q \approx 0.049$, equivalent to a duration of $P \times q \approx 3.6$ hr. The HATNet light curve for HAT-P-8 is plotted in Figure 3.

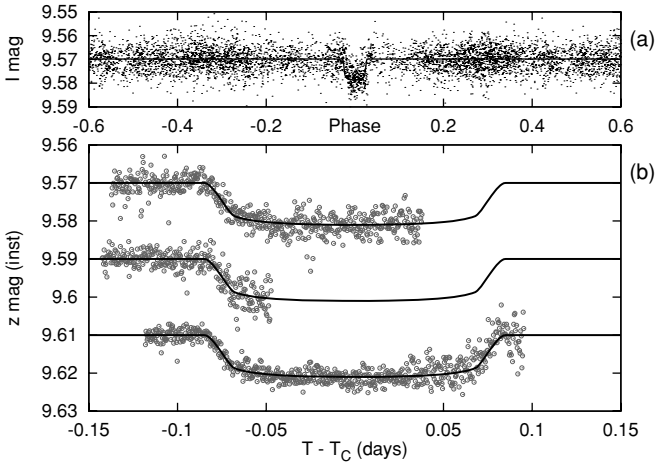

Figure 3. (a) Unbinned *I*-band light curve of HAT-P-8 combined from four HATNet telescopes, with 4460 points phased to the ephemeris derived in Section 4.4, with period $P = 3.0763776$ days. The superimposed curve shows the best model fit using quadratic limb darkening. (b) Unbinned Sloan *z*-band light curves from two partial and one complete transit events, acquired with KeplerCam on the FLWO 1.2 m telescope on 2007 October 29, November 1, and December 2. The best-fit transit model is superimposed.

4.2. Highly Precise Velocities

The initial spectroscopic reconnaissance of HTR205-024 with the CfA Digital Speedometer on the 1.5 m Tillinghast Reflector at FLWO on Mount Hopkins yielded 8 spectra over a period of 357 days and a mean velocity of -22.53 ± 0.79 km s^{-1} rms and $P(\chi^2) = 0.18$. Grids of correlations against our library of calculated synthetic spectra gave the best match for a template with $T_{\rm eff} = 6250$ K, $\log g = 4.0$, and $v \sin i = 12.8$ km s^{-1}. Encouraged by these positive results, we scheduled HTR205-024 for high-quality spectroscopic observations with HIRES (Vogt et al. 1994) on the Keck I telescope. Between 2007 August 24 and September 1, we obtained 10 exposures with an iodine cell, plus one iodine-free template, followed by 2 additional iodine observations on 2007 October 23 and November 23. The width of the spectrometer slit was 0.″86, resulting in a resolving power of $\lambda/\Delta\lambda \approx 55000$, while the wavelength coverage was $\sim$ 3800–8000 Å. The iodine gas absorption cell was used to superimpose a dense forest of I_2 lines on the stellar spectrum in order to establish an accurate wavelength fiducial (see Marcy & Butler 1992). Relative radial velocities in the solar system barycentric frame were derived as described by Butler et al. (1996), incorporating full modeling of

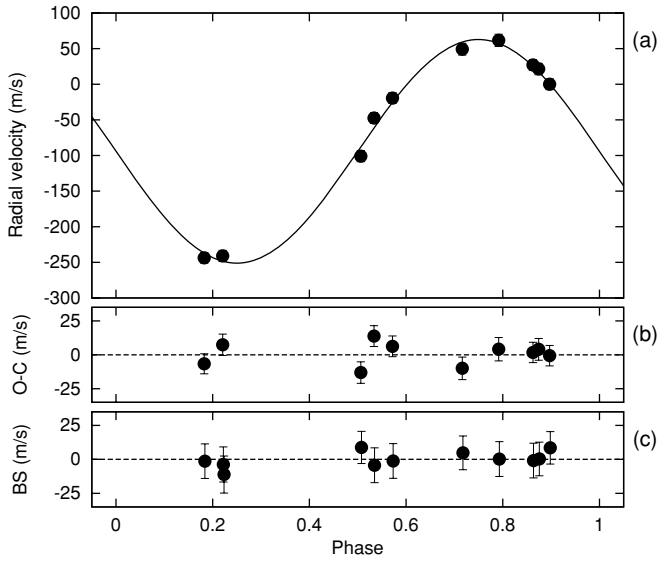

Figure 4. (a) Velocity curve for HAT-P-8 and the observed radial velocities obtained with Keck, using our orbital solution with the best period (see Section 4.4). The zero point of the radial velocities is relative to the Keck template spectrum. (b) Velocity residuals from the orbital solution (also see Section 4.4). The rms variation of the residuals is about 3.8 m s^{-1}. (c) Bisector spans (BS) for the 10 Keck spectra plus the single template spectrum, computed as described in the text. The mean value has been subtracted. Due to the relatively small errors compared to the radial velocity amplitude, the vertical scale in the (b) and (c) panels differs from the scale used in the panel (a).

the spatial and temporal variations of the instrumental profile. The final radial velocity data and their errors are listed in Table 9. The velocity curve for our orbital solution (see Section 4.4) is plotted in Figure 4(a), together with the observed velocities.

4.3. Photometric Follow-up Observations

To provide a high-quality light curve for HAT-P-8, KeplerCam on the 1.2 m telescope at FLWO was used to monitor two partial transit events and one complete event, on 2007 October 29, November 1, and December 2 UT, respectively; 526, 288, and 637 images in the Sloan z-band were obtained, all with exposure times of 15 s and cadence of 28 s. After correction of the images using bias and flat-field frames in the usual way, we derived a first-order astrometric transformation between the KeplerCam positions of $\sim$ 240 stars and the corresponding 2MASS positions, as described in Pál & Bakos (2006), yielding rms residuals of $\sim$ 0.4 pixel. Using these positions, we then performed aperture photometry using a series of apertures with radii of 4.0, 6.0, and 8.0 pixels for the first night; 4.5, 6.0, and 8.5 pixels for the second; and 10, 12, and 14 pixels for the third. Instrumental magnitude transformations were then obtained using $\sim$ 270 stars on a frame taken near culmination. First, we derived a transformation that was weighted by the estimated Poisson and background noise of each star. This led to an initial light curve and its associated rms for each star. We then performed the magnitude transformation again, this time weighting with the observed rms of the individual light curves. For each night, we chose the aperture that delivered the smallest rms photometric residuals for the OOT observations of HAT-P-8; 8, 8.5, and 12 pixels, respectively. The resulting light curves were then decorrelated against trends based on a simultaneous fit of the light-curve parameters and the parameters of the possible trends (see Section 4.4 for further details). This yielded

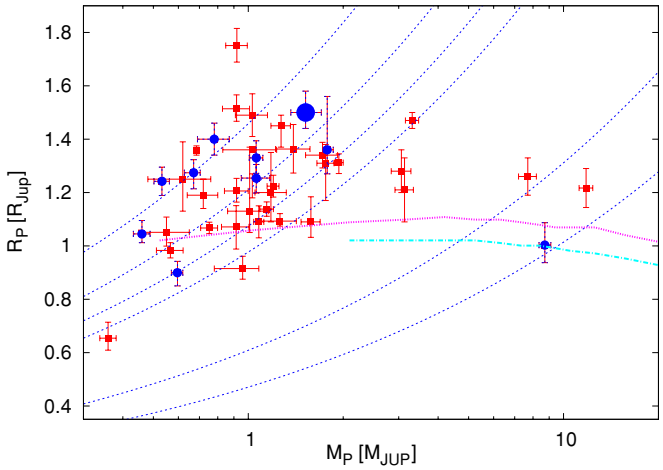

Figure 5. Mass–radius diagram for published transiting extrasolar planets. The data are taken from Torres et al. (2008) and www.exoplanet.eu. Filled circles mark HATNet discoveries, and the large filled circle marks HAT-P-8b. Overlaid are Baraffe et al. (2003; zero insolation planetary) isochrones for ages of 0.5 Gyr (upper, dotted line) and 5 Gyr (lower dash-dotted line), respectively. HAT-P-8b lies well above the average for Hot Jupiters.

(A color version of this figure is available in the online journal.)

Table 9
Relative Radial Velocity Measurements of HAT-P-8

BJD (2,454,000+)	Phase (−33+)	RV (m s^{-1})	σ_{RV} (m s^{-1})	BS (m s^{-1})	σ_{BS} (m s^{-1})
336.83041	0.2188	−240.9	4.3	−3.8	12.9
336.83906	0.2216	0.0	...	−11.1	13.7
337.79687	0.5329	−47.4	3.9	−4.3	12.8
337.91459	0.5712	−19.4	3.8	−1.2	12.8
338.80841	0.8618	+27.0	3.6	−0.9	12.8
338.91425	0.8962	0.0	3.6	+8.5	11.9
339.79280	1.1818	−243.7	3.4	−1.5	12.8
343.86602	2.5058	−100.9	4.4	+8.8	11.9
344.99747	2.8736	+21.4	4.6	+0.3	12.4
396.80973	19.7159	+49.3	5.0	+4.8	12.5
427.80583	29.7916	+61.6	5.5	+0.2	12.8

light curves with an overall rms of $\sim$ 2.3 mmag, for the first two nights and $\sim$ 1.9 mmag for the third night. These rms values are slightly larger than the predicted value of 1.4 mmag based on the photon noise (1.1 mmag) combined with the scintillation noise (0.8 mmag at airmass 1.3; see Dravins et al. 1998). The excess noise suggests that there may be modest residual trends that have not been removed. The light curves are shown in Figure 3(b). The time series for the HATNet and the KeplerCam photometry are published in full in the electronic version of this paper. The content and form of these data are illustrated in Tables 10 and 11.

4.4. Light Curve and Radial Velocity Analysis

The analysis of the available photometric and radial velocity data was performed as follows. First, we tested whether the orbit could be treated as circular, and fitted an eccentric orbit to the Keck/HIRES RV measurements by adjusting the Lagrangian orbital elements $k = e\cos\varpi$ and $h = e\sin\varpi$, along with the offset of the Keck/HIRES velocity system, (which is relative to the template exposure), and the velocity semi-amplitude, K. The orbital period was fixed to the value found from the HATNet light curves. We found that k and h are zero within nearly 1σ,

Table 10
HATNet Photometry for HTR205-024

BJD	Mag	Error
2453939.70260	9.57255	0.00461
2453939.70642	9.56319	0.00372
2453939.71020	9.56735	0.00358
2453939.71398	9.57243	0.00354
2453939.71777	9.56314	0.00364

Notes. Col. (1): Barycentric Julian Day, Col. (2): best detrended HATNet magnitude, Col. (3): estimated error in the best magnitude.

(This table is available in its entirety in a machine-readable form in the online journal. A portion is shown here for guidance regarding its form and content.)

Table 11
KeplerCam Photometry for HTR205-024

BJD	Mag	Error
2454403.69847	0.00311	0.00101
2454403.69883	0.00133	0.00104
2454403.69916	0.00580	0.00107
2454403.69949	0.00011	0.00103
2454403.69984	−0.01672	0.00111

Notes. Col. (1): Barycentric Julian Day, Col. (2): best detrended KeplerCam z magnitude, normalized to 0.0 out of transit, Col. (3): estimated error in the best magnitude.

(This table is available in its entirety in a machine-readable form in the online journal. A portion is shown here for guidance regarding its form and content.)

namely $k = 0.05 \pm 0.04$ and $h = -0.01 \pm 0.03$, justifying our assumption of a circular orbit for the subsequent analysis.

Following this, a joint fit was done using all of the available data, including the HATNet and the follow-up light curves, and the Keck radial velocities, i.e., we adjusted the transit timings, light-curve parameters, and the orbital parameters simultaneously to achieve the best fit to the entire data set. For the light-curve modeling, we assumed quadratic stellar limb darkening and we used the analytic formalism provided by Mandel & Agol (2002). The appropriate limb-darkening coefficients, $\gamma_1^{(z)}$, $\gamma_2^{(z)}$, $\gamma_1^{(I)}$ and $\gamma_2^{(I)}$, were derived using the stellar atmospheric parameters (see Section 4.5 for further details). The free parameters were the light-curve and orbital parameters, supplemented with the parameters of the possible systematics. Namely, the light-curve parameters were $T_{c,-485}$, the time of first transit center in the HATNet campaign; $T_{c,11}$, the time of the last observed transit center (on December 2); m, the OOT magnitude of the HATNet light curve in the I-band; the fractional planetary radius $p \equiv R_p/R_\star$; the square of the impact parameter b^2; and the quantity $\zeta/R_\star = (2\pi/P) \cdot (a/R_\star)/\sqrt{1-b^2}$, while the orbital parameters were the semi-amplitude of the radial velocity K and the center-of-mass velocity γ on the Keck system of relative velocities. The parameters of the systematics were the terms linear in airmass and hour angle (which are in practice equivalent with a linear and a quadratic term in time). The $\zeta/R_\star$ parameter is related to the duration of the transit as $(\zeta/R_\star)^{-1} = H$, where $2H$ is the time between the instants when the center of the planet crosses the limb of the star (i.e., $2H$ is approximately the "full width at half-maximum" of the transit, and is somewhat smaller than T_{14}, which is the time between the first and the last contact). For circular orbits, the impact parameter is related to the orbital inclination i as $b \equiv (a/R_\star)\cos i$. The parameters $\zeta/R_\star$ and b^2 were chosen instead of $a/R_\star$ and b because their correlations are negligible (see Pál 2008). We note that in this joint fit *all* of the transits in the HATNet light curve have been adjusted simultaneously, constrained by the assumption of a strictly periodic signal. The shape of all these transits was characterized by p, b^2, and $\zeta/R_\star$ (and the limb-darkening coefficients) while the distinct transit center time instants were interpolated using $T_{c,-485} = T_{c,first}$ and $T_{c,11} = T_{c,last}$. For the initial values we used the values provided by the BLS analysis, and the results provided by the fit of a sinusoidal function for the folded and phased RV data. We employed the method of refitting to synthetic data sets for error estimation which gives the *a posteriori* distribution of the adjusted values. For each individual χ^2 minimization, the downhill simplex algorithm has been utilized (aka "AMOEBA," see Press et al. 1992). The resulting parameter distribution was then used directly as an input to the stellar evolution modeling, discussed later in Section 4.5. We note that the joint fit also yielded the period of the planetary orbit, namely $P = (T_{c,11} - T_{c,-485})/496$, where 496 is the number of cycles between the first and last observed transit events.

Using the distribution of these parameters, it is straightforward to obtain the values and the errors of the additional derived parameters, e.g., $a/R_\star = (\zeta/R_\star)\sqrt{1-b^2}(P/2\pi)$.

4.5. Stellar Parameters

We used the iodine-free template spectrum from Keck for an initial determination of the atmospheric parameters. Spectral synthesis modeling was carried out using the SME software (Valenti & Piskunov 1996), with wavelength ranges and atomic line data as described by Valenti & Fischer (2005). We obtained the following initial values: effective temperature 6050 ± 70 K, surface gravity $\log g_\star = 3.97 \pm 0.10$ (cgs), iron abundance $[\mathrm{Fe/H}] = -0.08 \pm 0.05$, and projected rotational velocity $v \sin i = 11.6 \pm 0.5$ km s^{-1}. The uncertainties quoted here and in the remainder of this discussion are approximately twice the statistical uncertainties for the values given by the SME analysis. This reflects our attempt, based on prior experience, to account for possible systematic errors (e.g., Noyes et al. 2008; Valenti & Fischer 2005). Note that the previously discussed limb-darkening coefficients, $\gamma_1^{(z)}$, $\gamma_2^{(z)}$, $\gamma_1^{(I)}$ and $\gamma_2^{(I)}$ have been taken from the tables of Claret (2004) by interpolation to the above-mentioned SME values for $T_{\rm eff}$, $\log g_\star$, and [Fe/H].

The results of the joint fit, together with the initial results from spectroscopy enable us to refine the parameters of the star. As described by Sozzetti et al. (2007) and Torres et al. (2008), $a/R_\star$ is a better luminosity indicator than the spectroscopic value of $\log g_\star$, because the variation of stellar surface gravity has only a subtle effect on the line profiles. Therefore, we used the values of $T_{\rm eff}$ and [Fe/H] from the initial SME analysis, together with the distribution of $a/R_\star$ to estimate the stellar properties from comparison with the Yonsei-Yale (Y^2) stellar evolution models by Yi et al. (2001). As was discussed in Section 4.4, a Monte Carlo set for $a/R_\star$ values has been generated by the joint fit. We used this distribution for stellar evolution modeling as described in Pál et al. (2008). The set of the *a posteriori* distribution of the stellar parameters was therefore obtained, including the mass, radius, age, luminosity, and color (in multiple bands). Since the mass and radius (and their respective distributions) of the star are known, it is straightforward to obtain the surface gravity and its uncertainty together. The derived surface gravity was

Table 12
Stellar Parameters for HAT-P-8

Parameter	Value	Source
$T_{\rm eff}$ (K)	6200 ± 80	SME[a]
[Fe/H]	$+0.01 \pm 0.08$	SME
$v \sin i$ (km s^{-1})	11.5 ± 0.5	SME
$M_\star$ ($M_\odot$)	1.28 ± 0.04	Y^2+LC+SME[b]
$R_\star$ ($R_\odot$)	$1.58^{+0.08}_{-0.06}$	Y^2+LC+SME
$\log g_\star$ (cgs)	4.15 ± 0.03	Y^2+LC+SME
$L_\star$ ($L_\odot$)	$3.3^{+0.4}_{-0.3}$	Y^2+LC+SME
M_V (mag)	3.48 ± 0.12	Y^2+LC+SME
Age (Gyr)	3.4 ± 1.0	Y^2+LC+SME
Distance (pc)	230 ± 15	Y^2+LC+SME

Notes.
[a] SME = "Spectroscopy Made Easy" package for analysis of high-resolution spectra Valenti & Piskunov (1996). See the text.
[b] Y^2+LC+SME = Yale-Yonsei isochrones (Yi et al. 2001), light-curve parameters, and SME results.

$\log g_\star = 4.19^{+0.02}_{-0.04}$, which is somewhat larger than the previous value provided by the SME analysis. Therefore, we repeated the atmospheric modeling by fixing the surface gravity and letting only the other parameters vary. The next iteration of the SME analysis resulted in the following values: effective temperature $T_{\rm eff} = 6200 \pm 80$ K, metallicity [Fe/H] $= +0.01 \pm 0.08$, and projected rotational velocity $v \sin i = 11.5 \pm 0.5$ km s^{-1}. Based on these new spectroscopic values, we updated the limb-darkening coefficients and repeated the light curve and radial velocity simultaneous fit (except for the systematics parameters which were fixed here) plus the stellar evolution modeling in the same way as described in Section 4.4 and earlier in this subsection. The resulting stellar surface gravity was $\log g_\star = 4.15 \pm 0.03$, which is well within 1σ of the value obtained in the previous iteration. Therefore, we accept the values from the second joint fit and stellar evolution modeling as the final light-curve and stellar parameters (see Table 12).

The Yonsei-Yale isochrones also contain the absolute magnitudes and colors for different photometric bands from U up to M, providing an easy comparison of the estimated and the observed magnitudes and colors. Using these data, we determined the $V-I$ model color, $(V-I)_{\rm YY} = 0.58 \pm 0.02$. We have compared the $(V-I)_{\rm YY}$ color to published observational data, and found that our model color agrees well with the observed TASS color of $(V-I)_{\rm TASS} = 0.62 \pm 0.09$ (see Droege et al. 2006). Hence, the star is not affected by interstellar reddening within the errors, since $E(V-I) \equiv (V-I)_{\rm TASS} - (V-I)_{\rm YY} = 0.04 \pm 0.10$ (the galactic latitude of HAT-P-8 is $b = -21^\circ 22'$). For estimating the distance of HAT-P-8, we used the absolute magnitude $M_V = 3.48 \pm 0.12$ (resulting from the isochrone analysis, see also Table 12) and the $V_{\rm TASS} = 10.30 \pm 0.07$ observed magnitude. These two yield a distance modulus of $V_{\rm TASS} - M_V = 6.82 \pm 0.14$, i.e., a distance of $d = 230 \pm 15$ pc.

4.6. Excluding Blend Scenarios

Following Torres et al. (2007), we explored the possibility that the measured radial velocities are not real, but instead are caused by distortions in the spectral line profiles due to contamination from an unresolved eclipsing binary. In that case, the "bisector span" of the average spectral line should vary periodically with amplitude and phase similar to the measured velocities themselves (Queloz et al. 2001; Mandushev et al. 2005).

Table 13
Orbital and Planetary Parameters

Parameter	Value
Light-curve parameters	
P (days)	3.0763776 ± 0.000004
E (BJD $-$ 2,400,000)	$54,437.67582 \pm 0.00034$
T_{14} (days)[a]	0.1587 ± 0.0011
$T_{12} = T_{34}$ (days)[a]	0.0144 ± 0.0010
$a/R_\star$	$6.35^{+0.34}_{-0.17}$
$R_p/R_\star$	0.0953 ± 0.0009
$b \equiv a \cos i/R_\star$	$0.32^{+0.09}_{-0.19}$
i (deg)	$87.^\circ 5^{+1.9}_{-0.9}$
Spectroscopic parameters	
K (m s^{-1})	153.1 ± 3.9
γ (km s^{-1})	-22.53 ± 0.28
e	0 (adopted)
Planetary parameters	
M_p ($M_{\rm J}$)	$1.52^{+0.18}_{-0.16}$
R_p ($R_{\rm J}$)	$1.50^{+0.08}_{-0.06}$
$C(M_p, R_p)$	0.77
ρ_p (g cm^{-3})	0.568 ± 0.048
a (AU)	0.0487 ± 0.0026
$\log g_p$ (cgs)	3.23 ± 0.03
$T_{\rm eq}$ (K)	1700 ± 35
Θ	0.061 ± 0.003

Note.
[a] T_{14}: total transit duration, time between first to last contact; $T_{12} = T_{34}$: ingress/egress duration, namely the times between first and second, or third and fourth contact.

We cross-correlated each Keck spectrum against a synthetic template matching the properties of the star (i.e., based on the SME results, see Section 4.5), and averaged the correlation functions over all orders blueward of the region affected by the iodine lines. From this representation of the average spectral line profile we computed the mean bisectors, and as a measure of the line asymmetry we computed the "bisector spans" as the velocity difference between points selected near the top and the bottom of the mean bisectors (Torres et al. 2005). If the velocities were the result of a blend with an eclipsing binary, we would expect the line bisectors to vary in phase with the photometric period with an amplitude similar to that of the velocities. Instead, we detect no variation in excess of the measurement uncertainties (see Figure 4(c)). Therefore, we conclude that the velocity variations are real and that the star is orbited by a Jovian planet. We note here that the mean bisector span ratio relative to the radial velocity amplitude is the smallest (~ 0.026) among all the published HATNet planets, indicating an exceptionally high confidence that the RV signal is not due to a blend with an eclipsing binary companion.

4.7. Planetary and Orbital Parameters

As described in Pál et al. (2008), the planetary parameters and their uncertainties can be derived by the direct combination of the *a posteriori* distributions of the light-curve, radial velocity, and stellar parameters. The final planetary parameters are summarized at the bottom of Table 13.

5. DISCUSSION OF HAT-P-8b

Our newly confirmed planet HAT-P-8b has mass $M_{\rm p} = 1.52^{+0.18}_{-0.16}\ M_{\rm J}$ and radius $R_{\rm p} = 1.50^{+0.08}_{-0.06}\ R_{\rm J}$, which places it among the most inflated of the transiting Hot Jupiters currently

known (see Figure 5). The 3.3 $L_\odot$ luminosity of the host star and the $a = 0.0487 \pm 0.0026$ AU semimajor axis correspond to an equivalent semimajor axis of $a = 0.026$ AU if this object orbited our Sun and received the same flux. (Note, however, that the spectrum of the solar flux would be different). The theoretical radius from Fortney et al. (2008) would be $1.32R_J$, $1.25R_J$, and $1.17R_J$, respectively, for ages of 300 Myr, 1 Gyr, and 4.5 Gyr, assuming coreless models, and 0.02 AU orbital distance. HAT-P-8b with its $1.50^{+0.08}_{-0.06}$ R_J radius is thus inflated at the 2σ–3σ level, which is marginally significant. This result is also marginally consistent with Liu et al. (2008), where the 1.5 M_J mass and 0.026 AU equivalent solar distance yields such a large equilibrium radius only if the ratio between core heating power and insolation power is as high as 2×10^{-3}. The equilibrium timescale for the radius evolution would be very short, approximately 20 Myr. For comparison, WASP-5b (Anderson et al. 2008) has a similar mass (1.58 M_J), but its radius is only 1.09 R_J.

HAT-P-8b is also offset to the high-mass side of the period–mass relation. Planets with orbital periods similar to HAT-P-8b tend to have smaller masses, around 0.8 M_J as compared to the 1.52 M_J mass of HAT-P-8b. However, with the discovery of more massive planets, such as HAT-P-2b (Bakos et al. 2007a), XO-3b (Johns-Krull et al. 2008), and Corot-Exo-3b (Deleuil et al. 2008), the period–mass relation has become less clear-cut. Although the mass and radius of HAT-P-8b are larger than usual, together they imply an unremarkable surface gravity, $\log g = 3.23 \pm 0.03$ (cgs), and HAT-P-8b is consistent with the period–surface gravity relations reported by Southworth et al. (2007) and by Torres et al. (2008).

The Safronov number of HAT-P-8b is $\Theta = 0.061 \pm 0.003$, indicating that it belongs to the so-called Class I planets as defined by Hansen & Barman (2007). Curiously, HAT-P-8b lies at the very hot end of the distribution in the equilibrium temperature versus Safronov number diagram. All the hotter transiting planets are in Class II. Furthermore, while "inflated" planets mostly belong to Class II, HAT-P-8b has an inflated radius, yet belongs to Class I. With the recent discovery of several new transiting exoplanets, the Safronov dichotomy is becoming less pronounced, e.g., WASP-11b/HAT-P-10b (West et al. 2008; Bakos et al. 2008) falls in between the two groups, and the high- and low-mass exoplanets also seem to fall outside these groups.

The incident flux on HAT-P-8b is 1.91×10^9 erg s^{-1} cm^{-2}, placing it in the pM class, as defined by Fortney et al. (2008). This implies that HAT-P-8b has significant opacity due to the absorption by molecular TiO and ViO in its atmosphere, leading to a temperature inversion and a hot stratosphere. This could be tested with future observations from space. Based on its mass and incident flux, HAT-P-8b is similar to TrES-3 (O'Donovan et al. 2007).

HATNet operations have been funded by NASA grants NNG04GN74G, NNX08AF23G, and SAO IR&D grants. Work by G.Á.B. was supported by NASA through Hubble Fellowship Grant HST-HF-01170.01-A and by the Postdoctoral Fellowship of the NSF Astronomy and Astrophysics Program. We also acknowledge partial support from the Kepler Mission under NASA Cooperative Agreement NCC2-1390 (PI: D.W.L.). G.T. acknowledges partial support from NASA under grant NNG04LG89G, G.K. thanks the Hungarian Scientific Research Foundation (OTKA) for support through grant K-60750. This research has made use of Keck telescope time granted through NOAO (program A285Hr). This paper benefited from the comments of the referee.

REFERENCES

Anderson, D. R., Gillon, M., Hellier, C., Maxted, P. F. L., Pepe, F., Queloz, D., Wilson, D. M., & Collier Cameron, A. 2008, MNRAS, 387, L4
Bakos, G. Á., Lázár, J., Papp, I., Sári, P., & Green, E. M. 2002, PASP, 114, 974
Bakos, G. Á., Noyes, R. W., Kovács, G., Stanek, K. Z., Sasselov, D. D., & Domsa, I. 2004, PASP, 116, 266
Bakos, G. Á., et al. 2007a, ApJ, 670, 826
Bakos, G. Á., et al. 2007b, ApJ, 656, 552
Bakos, G. Á., et al. 2008, ApJ, 696, 1950
Bakos, G. Á., et al. 2009, ApJ, in press (arXiv:0901.0282)
Baraffe, I., Chabrier, G., Barman, T. S., Allard, F., & Hauschildt, P. H. 2003, A&A, 402, 701
Beatty, T. G., et al. 2007, ApJ, 663, 573
Brown, T. M., Rosing, W. E., Baliber, N., Hidas, M., & Street, R. 2007, BAAS, 38, 173
Butler, R. P., Marcy, G. W., Williams, E., McCarthy, C., Dosanjh, P., & Vogt, S. S. 1996, PASP, 108, 500
Claret, A. 2004, A&A, 428, 1001
Deleuil, M., et al. 2008, A&A, 491, 889
Dravins, D., Lindegren, L., Mezey, E., & Young, A. T. 1998, PASP, 110, 61
Droege, T. F., Richmond, M. W., Sallman, M. P., & Creager, R. P. 2006, PASP, 118, 1666
Fortney, J. J., Lodders, K., Marley, M. S., & Freedman, R. S. 2008, ApJ, 678, 1419
Hansen, B. M. S., & Barman, T. 2007, ApJ, 671, 861
Johns-Krull, C. M., et al. 2008, ApJ, 677, 657
Kovács, G., Bakos, G. Á., & Noyes, R. W. 2005, MNRAS, 356, 557
Kovács, G., Zucker, S., & Mazeh, T. 2002, A&A, 391, 369
Latham, D. W. 1992, in ASP Conf. Ser. 32, IAU Coll. 135, Complementary Approaches to Double and Multiple Star Research, ed. H. A. McAlister & W. I. Hartkopf (San Francisco, CA: ASP), 110
Latham, D. W. 2003, in ASP Conf. Ser. 294, Scientific Frontiers in Research on Extrasolar Planets, ed. D. Deming & S. Seager (San Francisco, CA: ASP), 409
Latham, D. W., Stefanik, R. P., Torres, G., Davis, R. J., Mazeh, T., Carney, B. W., Laird, J. B., & Morse, J. A. 2002, AJ, 124, 1144
Liu, X., Burrows, A., & Ibgui, L. 2008, ApJ, 687, 1191
Mandel, K., & Agol, E. 2002, ApJ, 580, L171
Mandushev, G., et al. 2005, ApJ, 621, 1061
Marcy, G. W., & Butler, R. P. 1992, PASP, 104, 270
McCullough, P. R., et al. 2006, ApJ, 648, 1228
Noyes, R. W., et al. 2008, ApJ, 673, L79
O'Donovan, F. T., et al. 2007, ApJ, 663, L37
Pál, A. 2008, MNRAS, 390, 281
Pál, A., & Bakos, G. Á. 2006, PASP, 118, 1474
Pál, A., et al. 2008, ApJ, 680, 1450
Press, W. H., Teukolsky, S. A., Vetterling, W. T., & Flannery, B. P. 1992, Numerical Recipes in C: The Art of Scientific Computing (2nd ed.; Cambridge: Cambridge Univ. Press)
Queloz, D., et al. 2001, A&A, 379, 279
Skrutskie, M. J., et al. 2006, AJ, 131, 1163
Southworth, J., Wheatley, P. J., & Sams, G. 2007, MNRAS, 379, 11
Sozzetti, A., Torres, G., Charbonneau, D., Latham, D. W., Holman, M. J., Winn, J. N., Laird, J. B., & O'Donovan, F. T. 2007, ApJ, 664, 1190
Torres, G., Konacki, M., Sasselov, D. D., & Jha, S. 2005, ApJ, 619, 558
Torres, G., Winn, J. N., & Holman, M. J. 2008, ApJ, 677, 1324
Torres, G., et al. 2007, ApJ, 666, L121
Valenti, J. A., & Fischer, D. A. 2005, ApJS, 159, 141
Valenti, J. A., & Piskunov, N. 1996, A&AS, 118, 595
Vogt, S. S., et al. 1994, Proc. SPIE, 2198, 362
West, R. G., et al. 2008, A&A, 502, 395
Winn, J. N., et al. 2007, AJ, 134, 1707
Yi, S. K., Demarque, P., Kim, Y.-C., Lee, Y.-W., Ree, C. H., Lejeune, T., & Barnes, S. 2001, ApJS, 136, 417
Zahn, J.-P. 1989, A&A, 220, 112
Zucker, S, & Mazeh, T. 1994, ApJ, 420, 806